

Article

CO and Propane Combustion on $\text{La}_{0.8}\text{Sr}_{0.2}\text{Co}_x\text{Fe}_{1-x}\text{O}_{3-\delta}$ Perovskites: Effect of Fe-to-Co Ratio on Catalytic Activity

Alexandros Safakas, Vasileios Ch. Kournoutis, Georgios Bampos  and Symeon Bebelis * 

Department of Chemical Engineering, University of Patras, Caratheodory 1, University Campus, GR-26504 Patras, Greece; asafakas@chemeng.upatras.gr (A.S.); vkournoutis@chemeng.upatras.gr (V.C.K.); geoba@chemeng.upatras.gr (G.B.)

* Correspondence: simeon@chemeng.upatras.gr; Tel.: +30-2610-969511

Abstract: Perovskites are promising alternative catalysts for oxidation reactions due to their lower cost compared to noble metals, and their greater thermal stability. The catalytic oxidation of CO is essential in order to control CO emissions in a series of applications whereas the catalytic combustion of propane is considered an economical and environmentally acceptable solution for energy production and gaseous pollutant management, since propane is among the organic compounds involved in photochemical reactions. This work concerns the effect of the Co/Fe ratio in the B-sites of a series of eight $\text{La}_{0.8}\text{Sr}_{0.2}\text{Co}_x\text{Fe}_{1-x}\text{O}_{3-\delta}$ perovskites, with x ranging from 0 to 1, on the catalytic activity towards CO and C_3H_8 oxidation. The perovskite oxides were synthesized using the combustion synthesis method and characterized with respect to their specific surface areas, structures, and reduction properties. Increasing the Co/Fe ratio resulted in an increase in CO and propane conversion under both oxidative and stoichiometric conditions. The increase in Co content is considered to facilitate the formation of oxygen vacancies due to the lower redox stability of the cobalt cations compared to iron cations, favoring oxygen ion mobility and oxygen exchange between the gas phase and the oxide surface, thus enhancing the catalytic performance.

Keywords: CO combustion; propane combustion; CO oxidation; propane oxidation; perovskites; $\text{La}_{0.8}\text{Sr}_{0.2}\text{Co}_x\text{Fe}_{1-x}\text{O}_{3-\delta}$; lanthanum strontium cobaltite ferrite



Citation: Safakas, A.; Kournoutis, V.C.; Bampos, G.; Bebelis, S. CO and Propane Combustion on $\text{La}_{0.8}\text{Sr}_{0.2}\text{Co}_x\text{Fe}_{1-x}\text{O}_{3-\delta}$ Perovskites: Effect of Fe-to-Co Ratio on Catalytic Activity. *Catalysts* **2023**, *13*, 1342. <https://doi.org/10.3390/catal13101342>

Academic Editor: Patrick Da Costa

Received: 30 June 2023

Revised: 19 September 2023

Accepted: 28 September 2023

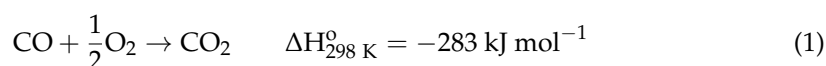
Published: 4 October 2023



Copyright: © 2023 by the authors. Licensee MDPI, Basel, Switzerland. This article is an open access article distributed under the terms and conditions of the Creative Commons Attribution (CC BY) license (<https://creativecommons.org/licenses/by/4.0/>).

1. Introduction

Increasing energy demands, mostly attributed to rising global population, result in an increase in the use of internal combustion engine vehicles that are considered as the main source of emissions of CO as well as other toxic compounds, such as NO_x , due to incomplete fossil fuel combustion [1]. These exhaust emissions are strongly related to a series of health issues and environmental problems [2,3]. The exhaust gas harmful components are reduced via oxidation in catalytic converters, using, typically, expensive noble metals as catalysts [4]. The oxidation of CO is described by the following equation [5]:



So far, the use of hybrid technology vehicles combining internal combustion engines with electric motors powered by batteries, and of electrical vehicles, powered exclusively by batteries or fuel cells with zero pollutant emissions [6], has not managed to reduce CO emissions to the desired levels, since the vast majority of human population does not have access to these advanced technologies. Nonetheless, the use of the aforementioned environmentally friendly technologies includes processes where CO production is inevitable. An indicative example is the production of significant amounts of CO in the hydrocarbons reforming processes for H_2 production to feed H_2 -fuelled proton exchange membrane fuel cells (PEMFCs) [7,8]. The reduction in CO concentration to the required level (<50 ppm) to

avoid poisoning of the Pt-based electrocatalysts typically used in PEMFCs is achieved via the water–gas shift reaction, followed by preferential oxidation of CO in the presence of H₂ [9].

Considering the above, the catalytic CO oxidation is essential in both conventional and alternative power applications. Catalysts typically used for CO oxidation are noble metal-based materials [10], which are characterized by high cost and low resistance to high CO concentration [11]. Towards addressing these issues, the development of alternative catalytic materials with enhanced resistance to CO poisoning, low cost, and similar activity to that of noble metal-based catalysts has attracted significant research interest [11,12].

Perovskite oxides of the ABO₃ type, where A-sites are occupied by alkaline earth or alkali metal cations and B-sites by transition metal cations, are considered as alternative catalytic materials for CO oxidation, exhibiting good activity and resistance to poisoning [12–14]. The chemical composition and structure of perovskite oxides play a crucial role in their catalytic performance [12–16], as they affect their redox [17,18] and/or acid–base [19] properties. The catalytic activity of a perovskite depends primarily on the transition metals occupying the B-sites, whereas A-sites are considered to play a secondary role in catalytic performance [12,13,20]. Perovskitic oxides with La or other rare earth metals in the A-sites and Co, Fe, Ni, or Mn in the B-sites have been reported as the most active for CO oxidation [12,16]. In addition to parameters that typically affect catalytic activity, such as the nature of the metal cations and the catalytic surface area [20], their enhanced catalytic performance has been attributed to structural defects and rapid surface oxygen exchange [12].

CO oxidation, as well as other oxidation reactions, on perovskite oxides can proceed via two different catalytic mechanisms, namely, the “suprafacial” and “intrafacial” mechanisms [12,14–16], which can also operate concurrently [21]. According to the suprafacial mechanism, CO or an organic molecule is oxidized by oxygen adsorbed on the catalytic surface from the gas phase, whereas the perovskite surface acts as a fixed template providing atomic orbitals with suitable energy and symmetry to facilitate the adsorption and surface reaction of the reactants. A Langmuir–Hinshelwood or an Eley–Rideal kinetic model can be used in this case, depending on whether the oxidized reactant is adsorbed or reacts directly from the gas phase. According to the intrafacial mechanism, which resembles the Mars–van Krevelen surface redox model [22], the lattice oxygen of the perovskite oxide participates in the CO or organic molecule oxidation step, and the reaction is carried out via a redox cycle where the consumed lattice oxygen is afterwards replenished by incorporation in the resultant surface oxygen vacancies of oxygen from the gas phase in the rate determining step. Provided that they have sufficient mobility, oxygen anions migrating from the bulk can also fill in the surface oxygen vacancies, thus virtually participating in the oxidation process, contrary to the suprafacial mechanism where only surface oxygen species participate in the reaction [14,16]. In general, the suprafacial mechanism is expected for low-temperature processes in which removal/incorporation of oxygen from/into the perovskite lattice is much slower than adsorption/desorption and reactions between adsorbed surface species [14–16]. The intrafacial mechanism, on the other hand, is preferably followed at relatively higher temperatures, where the mobility of lattice oxygen and the surface oxygen exchange are favored [14–16].

Partial substitution of the metal cations at the A- and B-sites with metal cations of different oxidation numbers results in alteration of the oxygen sub-stoichiometry with parallel formation of vacant lattice sites or/and change in the oxidation state of the transition metal ions at the B-sites or/and formation of positively charged holes in order to maintain overall electro-neutrality, while the perovskitic structure remains stable [5,14]. This modification can enhance the catalytic performance of the perovskite oxide. For example, in La_{1-x}Sr_xMnO₃ perovskites, the La³⁺ cations are partially substituted by Sr²⁺ cations at the A-sites, causing a deviation from the electro-neutrality, which is counterbalanced by partial transformation of Mn³⁺ to Mn⁴⁺ at the B-sites [5]. On the other hand, in La_{1-x}Sr_xFeO₃ perovskites, partial substitution of lanthanum by strontium at the A-sites is

followed by the formation of oxygen vacancies as the main mechanism to maintain overall electro-neutrality [23,24]. In general, partial substitution of both A- and B-sites in a ABO_3 perovskite by an alkaline earth metal A' and another transition metal B', respectively, to form a $AA'BB'O_3$ type perovskite, results both in change in the oxidation state of the metal ions at the B-sites and in the formation of lattice oxygen vacancies, facilitating oxygen dissociation on the surface, increasing lattice oxygen anion mobility, and improving the ionic conductivity of the parent material [14,25].

Combining two catalytically active transition metals at the B-sites of a perovskitic oxide can result in enhanced catalytic activity owing to a synergistic effect between the two metals, which alters the adsorptive properties of the perovskite [5]. Co, Mn, and Fe cations are typically found at the B-sites of the perovskite catalysts [5]. It is generally accepted that the co-presence of cations of two different transition metals at the B-sites facilitates electron transfer in the redox catalytic cycle, which enhances the reducibility of the perovskite oxide and improves its catalytic performance [5]. Zhang et al. [26] used oxygen temperature-programmed desorption (O_2 -TPD) to study the effect of partial substitution of La by Sr and Co by Fe at the A- and B-sites, respectively, on the desorption properties of the perovskite $La_{1-x}Sr_xCo_{1-y}Fe_yO_3$. They found that coexistence of Co and Fe was beneficial for the oxygen adsorption/desorption properties of the perovskite, thus enhancing its catalytic activity towards n-butane complete oxidation. Oxygen adsorption/desorption at temperatures lower than 300 °C was favored whereas partial substitution of La by Sr at the A-sites significantly enhanced the activity of the perovskite. Scott et al. [27] studied the effect of temperature, chemical composition, and oxygen partial pressure on oxygen sub-stoichiometry δ of $La_{1-x}Sr_xCo_{1-y}Fe_yO_{3-\delta}$. They found that δ increased with increasing temperature, decreasing oxygen partial pressure, and increasing Sr and Co content at the A- and B-sites, respectively. Lankhorst and ten Elshof [28] investigated the effect of partial substitution of Co by Fe at the B-sites of $La_{0.2}Sr_{0.8}Co_{1-y}Fe_yO_{3-\delta}$ ($y = 0-0.6$) on oxygen sub-stoichiometry δ and found that the δ value decreased with increasing Fe/Co ratio. This was attributed to an increase in the binding energy of O^{2-} in the perovskite lattice, which favors the formation of holes over oxygen vacancies [28].

Levasseur and Kaliaguine [29] studied the effect of the Co/Fe ratio at the B-sites of $La_{1-x}Ce_xCo_{1-y}Fe_yO_3$ ($x = 1, 0.9$ and $y = 0, 0.2, 0.4, 1$) on catalytic activity for methanol, CO, and CH_4 oxidation. Partial substitution of La by Ce at the A-sites caused an enhancement of the catalytic performance. Increasing Fe content resulted in a decrease in the catalytic activity and in a decrease in the β -oxygen peak in the O_2 -TPD curves, accompanied by a shift in the desorption peaks of all oxygen species to higher temperatures. Moreover, decreasing the Co/Fe ratio resulted in an increase in the reduction temperature of Co^{3+} and Co^{2+} species to Co^{2+} and Co^0 species, respectively, as manifested by H_2 temperature-programmed reduction measurements. Therefore, it was concluded that an increase in the Fe content reduces the redox activity of the B-sites and decreases the lattice oxygen mobility. Similar results were reported by Tanaka et al. [30] concerning the catalytic activity towards the oxidation of a mixture of hydrocarbons, NO, and CO over $La_{0.9}Ce_{0.1}Co_{1-y}Fe_yO_3$ ($y = 0, 0.2, 0.4, 0.6, 0.8, 1$). Isupova et al. [31] observed a maximum CO oxidation activity of $La_{0.7}Sr_{0.3}Co_{1-y}Fe_yO_3$ ($y = 0, 0.05, 0.1, 0.7$) for a Co/Fe atomic ratio equal to 0.95/0.05. This behavior was attributed to an increase in the number of structural defects which in turn resulted in an increase in the density of surface defects, thus favoring CO oxidation reaction on the basis of its mechanism.

Catalytic combustion of propane, described by Equation (2), is also a reaction of significant research interest, both for energy production, especially in areas where there is no access to natural gas, and for management of air pollutants since propane belongs to volatile organic compounds (VOCs) [32].



Noble metal-based catalysts are considered highly efficient towards propane combustion and have been extensively studied [33–38]. However, the high cost of noble metals has motivated the development of alternative noble metal-free catalytic systems. Ma et al. [39]

investigated propane oxidation on Co_3O_4 nanorods, as alternative to $\text{Pt}/\text{Al}_2\text{O}_3$. They highlighted the differences in propane combustion mechanism over the two catalysts, reporting a Langmuir–Hinshelwood mechanism for Co_3O_4 nanorods and an Eley–Rideal mechanism for $\text{Pt}/\text{Al}_2\text{O}_3$. Perovskites have also been used as catalysts for propane combustion, although the corresponding studies are significantly fewer than those concerning CO oxidation [14]. Klvana et al. [40] investigated the effect of the synthesis method of $\text{La}_{0.66}\text{Sr}_{0.34}\text{Co}_{0.2}\text{Fe}_{0.8}\text{O}_3$ and specific surface area on its activity for propane combustion. Kinetic experiments over a wide range of gas phase compositions indicated a Mars–van Krevelen mechanism [22,40,41]. Alifanti et al. [42] compared methane and propane oxidation on $\text{La}_{1-x}\text{Sr}_x\text{M}_{1-y}\text{M}'_y\text{O}_{3-\delta}$ (M: Mn, Cu, Ni, Co and M': Ni, Fe), focusing on the relative role of specific surface area and oxygen mobility. The effect of partial substitution of La by Sr, Ce, and Ca at the A-sites has been studied in propane oxidation on $\text{La}_{1-x}\text{Sr}_x\text{CoO}_3$ [43], on $\text{La}_{1-x}\text{Sr}_x\text{FeO}_3$, $\text{La}_{1-x}\text{Ce}_x\text{FeO}_3$ and $\text{La}_{1-x}\text{Ce}_x\text{CoO}_3$ [44], and on $\text{La}_{1-x}\text{Ca}_x\text{CoO}_3$ [25]. Merino et al. [45] studied the effect of the partial substitution of Co by Fe at the B-sites in propane combustion on $\text{LaCo}_{1-y}\text{Fe}_y\text{O}_{3\pm\lambda}$ ($y = 0, 0.1, 0.3, 0.5$). Partial substitution of Co by Fe by 10% ($y = 0.1$) was found to favor the catalytic performance, whereas a further increase in the Fe content resulted in a gradual reduction in the catalytic activity [45]. Song et al. [46] investigated the kinetics of propane oxidation on $\text{La}_{0.66}\text{Sr}_{0.34}\text{Ni}_{0.3}\text{Co}_{0.7}\text{O}_3$ and proposed an extended Mars–van Krevelen kinetic model, taking also into account the inhibiting effect of adsorbed CO_2 and H_2O products.

Considering the abovementioned studies of CO and propane combustion on perovskite oxides, it can be concluded that relevant research interest has been mainly focused on the investigation of the catalytic effect of the transition metals occupying the B-sites, with particular interest in Co and Fe. Along this direction, eight (8) perovskite oxides $\text{La}_{0.8}\text{Sr}_{0.2}\text{Co}_x\text{Fe}_{1-x}\text{O}_{3-\delta}$, with a fixed La/Sr ratio at the A-sites and a varying Co and Fe content at the B-sites ($x = 0, 0.1, 0.2, 0.4, 0.6, 0.8, 0.9, 1$) were synthesized via the combustion synthesis method and tested for their catalytic activity towards CO and propane combustion. The synthesized oxides were characterized as it concerns their specific surface area, structure, and reducibility in H_2 atmosphere. The observed differences in catalytic activity among the tested perovskites were mainly correlated with differences in oxygen vacancies, surface oxygen exchange, and oxygen ion mobility induced by changing the relative content of Co and Fe at the B-sites. The novelty of the present work lies on the fact that, to the best of our knowledge, it is the first systematic study of the effect of the Co/Fe ratio on the catalytic performance of La-Sr-Co-Fe perovskites for both CO and propane total oxidation, two reactions of significant environmental and technological interest, allowing comparison of the activity trends for the two reactions.

2. Results

2.1. Physicochemical and Structural Characterization

The composition, the notation, and the measured via N_2 physical adsorption (BET method) SSA values of the synthesized perovskites are shown in Table 1. No significant differences were observed between their nominal composition and their stoichiometry determined via inductively coupled plasma optical emission spectroscopy (ICP-OES). The SSA varied from $4.1 \text{ m}^2 \text{ g}^{-1}$ for LSCF_8291 to $7.9 \text{ m}^2 \text{ g}^{-1}$ for LSCF_8219. The low SSAs are attributed to the elevated calcination temperature ($900 \text{ }^\circ\text{C}$) used to obtain the perovskite structure [47].

The XRD spectra of the eight synthesized perovskites are presented in Figure 1. Six of them (LSC, LSCF_8282, LSCF_8264, LSCF_8246, LSCF_8228, and LSF) have been already presented in a previous work of our group [47]. After identification of the formed phases using ICDD data files, the formation of the perovskite phase was confirmed (main peak at 2θ between 32° and 34°) without the presence of secondary phases at detectable levels. A gradual shift in all XRD peaks towards lower 2θ values was observed with increasing partial substitution of Co by Fe (Figure 1b). This shift was accompanied by a change in the main peak from doublet ($0.4 \leq x \leq 1$) to single ($x = 0, 0.1, 0.2$), indicating a change in the $\text{La}_{0.8}\text{Sr}_{0.2}\text{Co}_x\text{Fe}_{1-x}\text{O}_{3-\delta}$ perovskite structure from rhombohedral to orthorhombic [25,48,49].

This is in accordance with the results of Tai et al. [49] for $\text{La}_{0.8}\text{Sr}_{0.2}\text{Co}_{1-y}\text{Fe}_y\text{O}_3$ ($0 \leq y \leq 1$) sintered in air at 1250 to 1350 °C, who reported that partial substitution of Co by Fe to an iron percentage of 80% or higher ($y = 0.8, 0.9, 1$) resulted in a change in the perovskite unit cell from rhombohedral to orthorhombic. Similarly, Natile et al. [48] reported a change from rhombohedral to orthorhombic structure for $\text{La}_{0.6}\text{Sr}_{0.4}\text{Co}_{1-y}\text{Fe}_y\text{O}_{3-\delta}$ perovskites ($y = 0.2, 0.5, 0.8$) calcined at 800 °C, but for a lower Fe content ($y \geq 0.5$), which implies that the La/Sr ratio at the A-sites and, possibly, the thermal treatment conditions can affect the Co/Fe ratio for which the aforementioned change in unit cell geometry occurs. The observed gradual shift in the XRD peaks towards higher 2θ values with increasing partial substitution of Fe by Co (Figure 1) indicates a contraction of the perovskite unit cell, which can be attributed to the substitution of Fe^{3+} by Co^{3+} , the latter having a smaller ionic radius [45,48,50]. Moreover, this shift becomes relatively smaller with increasing Co content (Figure 1b), which implies a smaller reduction in the unit cell size [47]. This behavior has also been reported for $\text{LaCo}_x\text{Fe}_{1-x}\text{O}_{3-\delta}$, associated with changes in the relative number of Co^{2+} to Co^{3+} and Fe^{4+} to Fe^{3+} accompanying the substitution of Fe^{3+} by Co^{3+} [50].

Table 1. Composition, notation, specific surface area (SSA), and average crystallite size of the synthesized perovskites $\text{La}_{0.8}\text{Sr}_{0.2}\text{Co}_x\text{Fe}_{1-x}\text{O}_{3-\delta}$.

Perovskite	Notation	SSA ($\text{m}^2 \text{g}^{-1}$)	Crystallite Size (nm)
$\text{La}_{0.8}\text{Sr}_{0.2}\text{FeO}_{3-\delta}$	LSF	7.2 ¹	29.1
$\text{La}_{0.8}\text{Sr}_{0.2}\text{Co}_{0.1}\text{Fe}_{0.9}\text{O}_{3-\delta}$	LSCF_8219	7.9	19.7
$\text{La}_{0.8}\text{Sr}_{0.2}\text{Co}_{0.2}\text{Fe}_{0.8}\text{O}_{3-\delta}$	LSCF_8228	5.6 ¹	16.9
$\text{La}_{0.8}\text{Sr}_{0.2}\text{Co}_{0.4}\text{Fe}_{0.6}\text{O}_{3-\delta}$	LSCF_8246	4.7 ¹	50.2
$\text{La}_{0.8}\text{Sr}_{0.2}\text{Co}_{0.6}\text{Fe}_{0.4}\text{O}_{3-\delta}$	LSCF_8264	6.8 ¹	32.5
$\text{La}_{0.8}\text{Sr}_{0.2}\text{Co}_{0.8}\text{Fe}_{0.2}\text{O}_{3-\delta}$	LSCF_8282	5.5 ¹	32.5
$\text{La}_{0.8}\text{Sr}_{0.2}\text{Co}_{0.9}\text{Fe}_{0.1}\text{O}_{3-\delta}$	LSCF_8291	4.1	60.2
$\text{La}_{0.8}\text{Sr}_{0.2}\text{CoO}_{3-\delta}$	LSC	5.7 ¹	34.2

¹ ref. [47].

The average crystallite size, estimated via application of the Scherrer equation [51,52] for the XRD peak located at 2θ between 46° and 48°, revealed a significant difference among the synthesized materials (Table 1). The largest crystallite size, equal to 60.2 nm, was calculated for LSCF_8291, whereas the smallest, equal to 16.9 nm, was calculated for LSCF_8228. Although no clear trend was observed, it could be argued that increasing the Fe content results in an increase in the SSA and a decrease in the average crystallite size, as also reported for $\text{La}_{0.6}\text{Sr}_{0.4}\text{Co}_{1-y}\text{Fe}_y\text{O}_{3-\delta}$ by Natile et al. [48]. The observed changes in the crystallite size were accompanied by changes in the lattice strain, ϵ (%), which was calculated using the Williamson–Hall method [52,53]. Specifically, the calculated lattice strain values for the synthesized perovskites follow the increasing order, LSCF_8291 (0.14%) < LSCF_8246 (0.15%) < LSC (0.24%) < LSCF_8282 (0.25%) < LSCF_8264 (0.26%) < LSF (0.28%) < LSCF_8219 (0.38%) < LSCF_8228 (0.4%), which corresponds to a decreasing order of crystallite size (Table 1).

2.2. Investigation of the Perovskite Reducibility

The synthesized perovskites were characterized with respect to their reducibility using H_2 temperature-programmed reduction (H_2 -TPR). The recorded mass spectrometer signal (ms signal) for H_2 ($m/z = 2$) as a function of temperature (TPR profile) is shown in Figure 2 for all tested samples. The main feature of the TPR curves is a broad inverse peak that starts to develop at temperatures between ca. 200 °C and 250 °C depending on the perovskite composition and which seems to consist of more than one peak, clearly for Co/Fe ratio in the range 6/4 to 1/9. For Co/Fe ratios larger than 6/4, additional reduction features appear at temperatures higher than ca. 595 °C that were not completed due to limitations of the experimental setup, with the exception of a peak located between ca. 595 °C and 685 °C in the TPR profile of the LSC oxide.

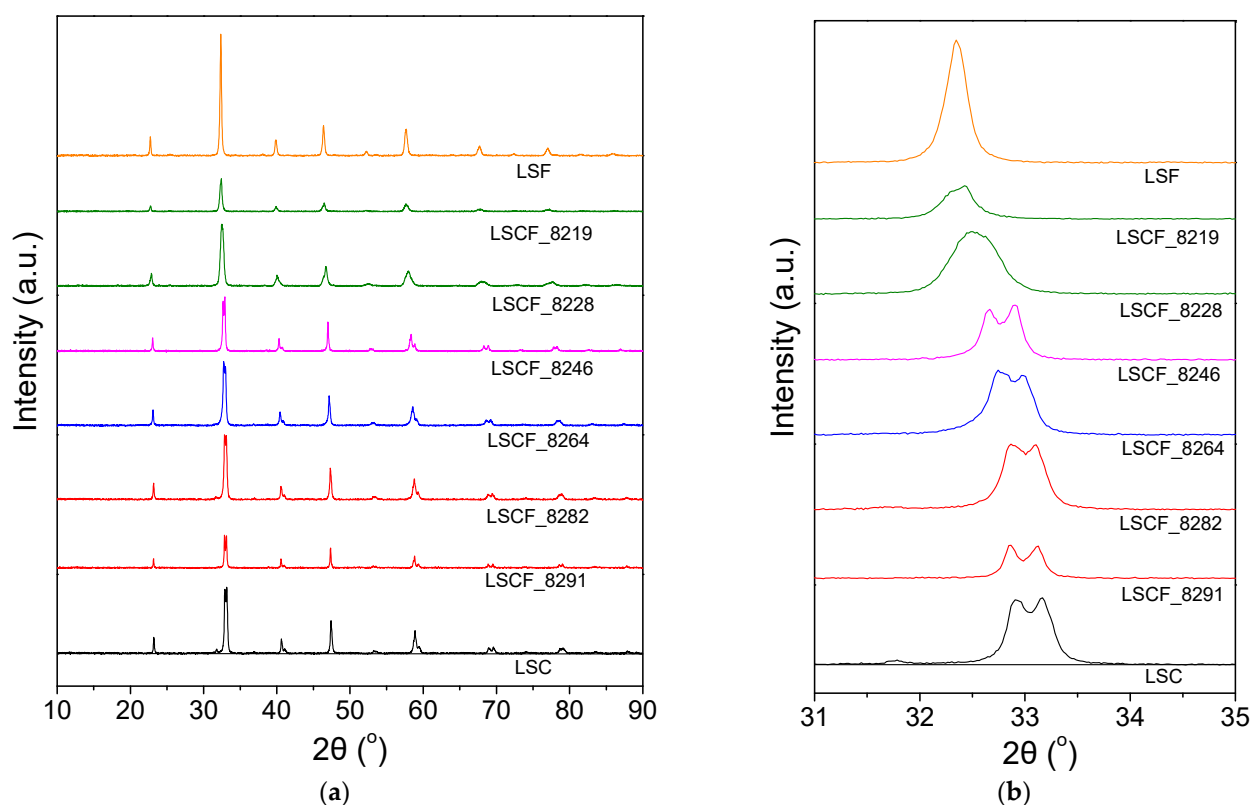


Figure 1. (a) XRD patterns of the synthesized perovskite oxides. (b) Detailed view of the XRD patterns in the 2θ range from 31° to 35° .

Interpretation of the H_2 -TPR features of LSCF perovskite oxides depends on the temperature range of their appearance. The reduction of Fe is typically performed in two consecutive steps, i.e., reduction of Fe^{4+} to Fe^{3+} at 350 to $450^\circ C$ and subsequent reduction of Fe^{3+} to Fe^{2+} and possibly further reduction to metallic Fe^0 , at temperatures higher than $500^\circ C$ [54]. The reduction of cobalt cations is also carried out in two steps, Co^{3+} being reduced to Co^{2+} and Co^{2+} to Co^0 at temperatures lower and higher than $500^\circ C$, respectively [54]. However, according to García-López et al. [55], the reduction of Fe^{3+} to Fe^{2+} can take place at temperatures lower than $400^\circ C$ or in the temperature range where reduction of Co^{3+} occurs, resulting in overlapping of the corresponding TPR peaks. Merino et al. [45] also observed, in TPR profiles of $LaCo_{1-y}Fe_yO_3$ oxides, the appearance of a peak in the temperature range 355 – $385^\circ C$, which they attributed to the reduction of the Fe^{4+} species.

In the present work, broad reduction peaks were recorded for all tested perovskites that could be explained by the potential participation of the bulk lattice oxygen in the reduction reactions, since the surface oxygen is consumed rapidly with increasing temperature. As shown in Figure 2, the increase in the Co/Fe ratio (from LSF to LSC) was accompanied by a shift in the onset reduction temperature to lower values. This can be attributed to the facilitation of the surface lattice oxygen release, associated with the lower redox stability of cobalt cations in LSCF compared to iron cations [56,57]. Moreover, the parallel increase in the number of oxygen ion vacancies and oxygen ion mobility [12,14,58] facilitates the bulk lattice oxygen diffusion to the oxide surface, thus favoring the reaction with hydrogen. The appearance of a doublet peak for LSCF_8219 to LSCF_8264 can be associated with the onset of the reduction of Co^{3+} to Co^{2+} , occurring parallel to the reduction of Fe^{4+} to Fe^{3+} [45]. For LSCF_8282 and LSCF_8291, the peak associated with the reduction of Fe^{4+} to Fe^{3+} is not discernible, as it is presumably overlapped by the dominant peak associated with the reduction of Co^{3+} to Co^{2+} [45].

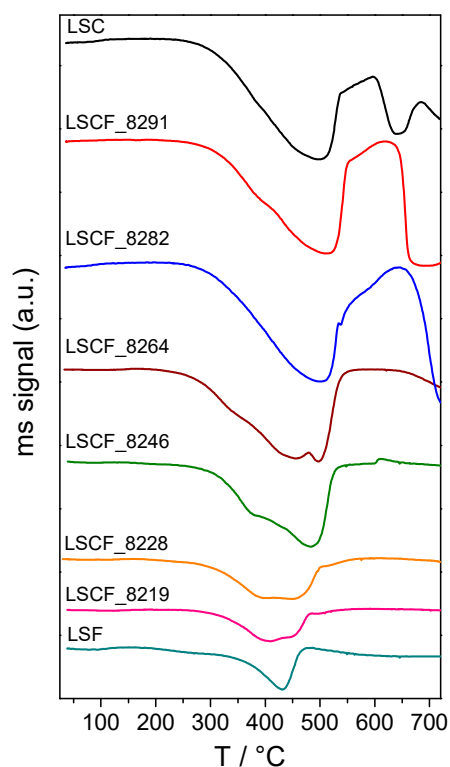


Figure 2. H₂ temperature-programmed reduction profiles of the synthesized perovskites.

2.3. Catalytic Activity for CO Combustion

In Figure 3a, the CO conversion (X_{CO}) vs. temperature curves obtained under oxidative conditions (feed composition: 1% CO/5% O₂/balance He) for the synthesized perovskites are presented. As shown in the figure, complete CO conversion was achieved for all oxides in the temperature range between 265 °C and 460 °C, whereas at each temperature conversion increased with increasing Co/Fe ratio at the B-sites. In Figure 3b, the light-off temperatures T_{50} for the tested materials, i.e., the temperatures corresponding to a CO conversion equal to 50%, are compared. Increasing the Co/Fe ratio resulted in a gradual decrease in T_{50} , which was more pronounced for Co/Fe ratios equal or smaller than 6/4. As shown in the figure, the T_{50} value was practically the same for the LSCF_8264, LSCF_8282, and LSCF_8291 perovskites, which is also evident by comparing the corresponding CO conversion curves (Figure 3a).

Figure 3c shows, in the form of Arrhenius plots, the temperature dependence of the CO₂ production rate r_{CO_2} for the tested perovskites, under oxidative conditions. The CO₂ production rate was measured under practically differential conditions and was normalized to the SSA of each sample to take into account the existing differences in the specific surface area of the tested catalysts (Table 1) and compare their intrinsic activity, assuming that the change in the number of active sites follows the change in SSA. By increasing the Co/Fe ratio, the same r_{CO_2} was achieved at lower temperatures, which implies enhancement of the intrinsic catalytic activity. In order to highlight the differences in the intrinsic catalytic activity of the tested perovskites, the temperatures corresponding to r_{CO_2} equal to 10^{-7} mol s⁻¹ m⁻² (Figure 3c) are compared in Figure 3d. As shown in the figure, this temperature decreased from 283 °C for LSF to 116 °C for LSC, indicating that among the tested perovskites (Table 1) LSC and LSF were the most active and the less active, respectively, for CO oxidation in terms of intrinsic activity, in agreement with the conclusions drawn by comparing the T_{50} values (Figure 3b).

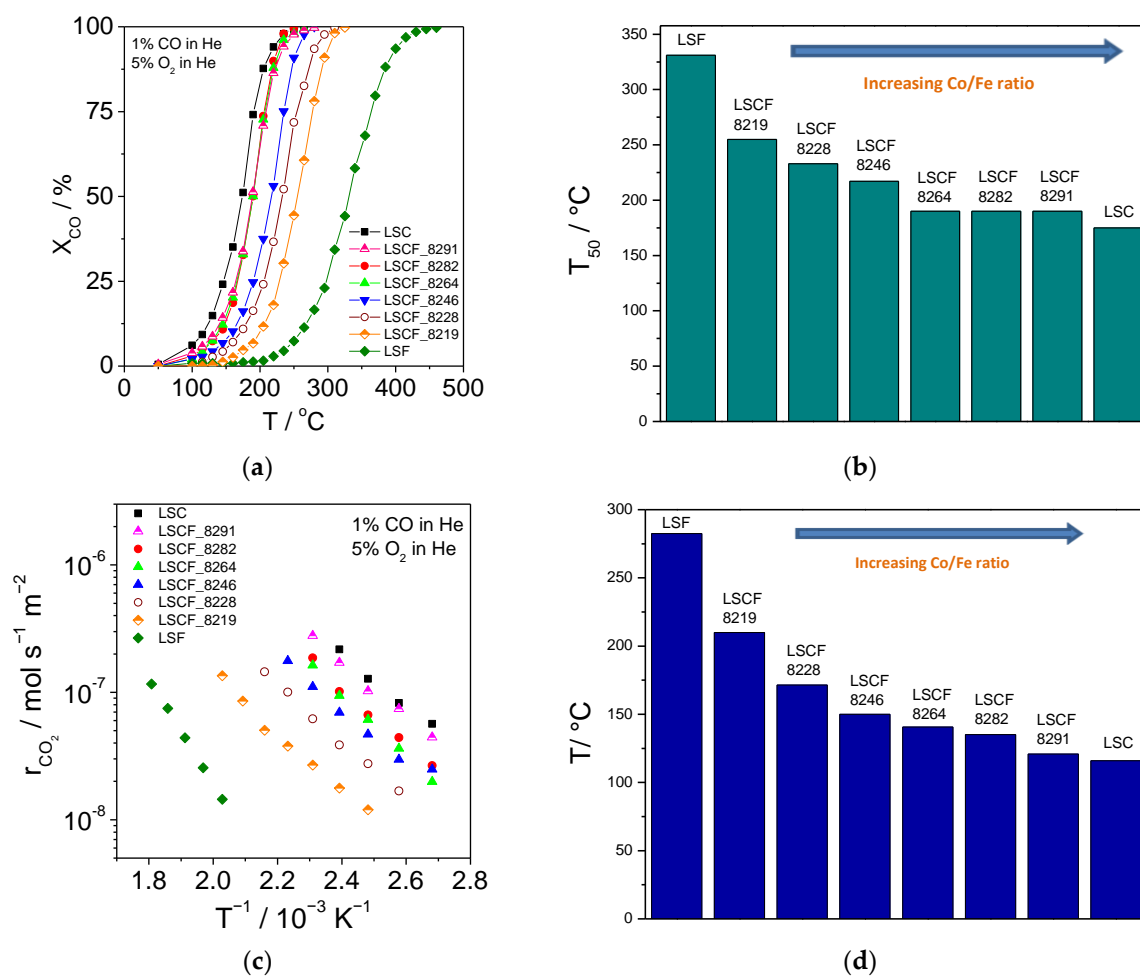


Figure 3. CO combustion on $\text{La}_{0.8}\text{Sr}_{0.2}\text{Co}_x\text{Fe}_{1-x}\text{O}_{3-\delta}$ perovskites for oxidative feed conditions (1%CO/5%O₂/balance He): (a) CO conversion, X_{CO} , as a function of temperature, and (b) comparison of the corresponding light-off temperatures, T_{50} . (c) Temperature dependence of the CO₂ production rate, r_{CO_2} (Arrhenius plots), measured under practically differential conditions, and (d) comparison of the temperatures corresponding to r_{CO_2} equal to $10^{-7} \text{ mol s}^{-1} \text{ m}^{-2}$.

In Figure 4, the catalytic performance of the synthesized $\text{La}_{0.8}\text{Sr}_{0.2}\text{Co}_x\text{Fe}_{1-x}\text{O}_{3-\delta}$ perovskites for CO combustion under stoichiometric feed conditions (1% CO/0.5% O₂/balance He) is compared. Figure 4a shows the dependence of CO conversion (X_{CO}) on temperature. As shown in the figure, complete conversion of CO is reached for temperatures ranging between ca. 430 °C and 640 °C, which are considerably higher than the corresponding ones for oxidative feed conditions (Figure 3a). This difference implies a positive reaction order with respect to oxygen, considering the much lower percentage of O₂ in the feed under stoichiometric conditions (0.5%) compared to that under oxidative conditions (5%). As in the latter case, decreasing the Fe content at the B-sites of the LSCF perovskites resulted in an increase in the CO conversion for the same temperature for $\text{Co/Fe} \leq 6/4$, whereas for higher Co/Fe ratios, the differences in CO conversion were small (Figure 4a). Similarly, as shown in Figure 4b, T_{50} decreased from ca. 325 °C for the LSF to ca. 200 °C for the LSCF_8264 and remained practically constant by further decreasing the Fe content (with parallel increase in the Co content) to zero (LSC sample).

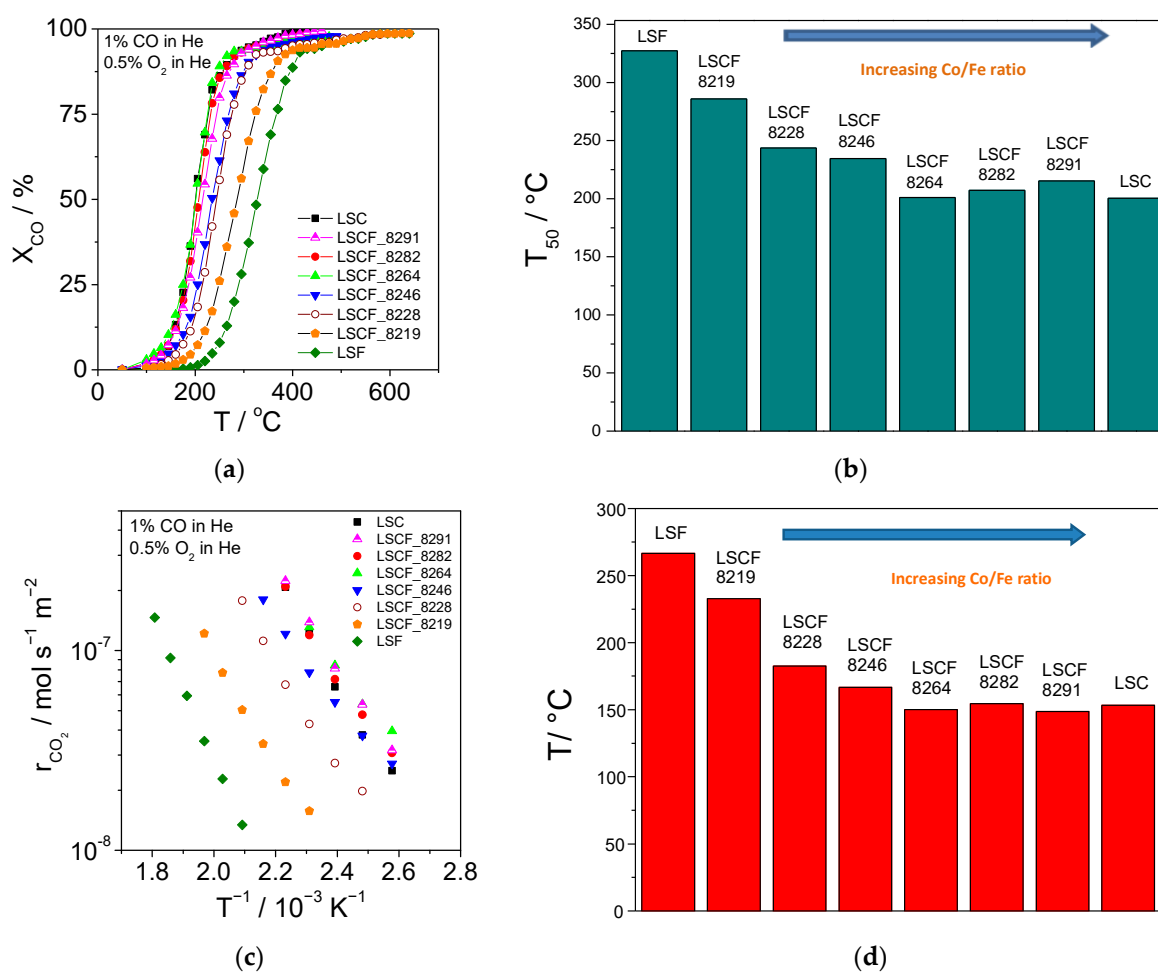


Figure 4. CO combustion on $La_{0.8}Sr_{0.2}Co_xFe_{1-x}O_{3-\delta}$ perovskites for stoichiometric feed conditions (1% CO/0.5% O₂/balance He): (a) CO conversion, X_{CO} , as a function of temperature, and (b) comparison of the corresponding light-off temperatures, T_{50} . (c) Temperature dependence of the CO₂ production rate, r_{CO_2} (Arrhenius plots), measured under practically differential conditions, and (d) comparison of the temperatures corresponding to r_{CO_2} equal to 10^{-7} mol s⁻¹ m⁻².

Figure 4c shows, in the form of Arrhenius plots, the temperature dependence of r_{CO_2} for the tested perovskites, as measured under practically differential conditions and for a stoichiometric CO/O₂ ratio in the feed (1% CO/0.5% O₂/balance He). By increasing the Co/Fe ratio up to 6/4, the same r_{CO_2} was obtained at lower temperatures, indicating an increase in the intrinsic catalytic activity, whereas for higher Co/Fe ratios, the effect was not significant (Figure 4c). This is clearly shown in Figure 4d, where the temperatures corresponding to r_{CO_2} equal to 10^{-7} mol s⁻¹ m⁻² are presented. As shown in the figure, this rate value was obtained at 267 °C for LSF and at 150 °C for LSCF_8264, whereas for the perovskite oxides with higher Co/Fe ratios, the corresponding temperature remained practically constant, varying between 150 and 154 °C (Figure 4d).

In Figure 5, the catalytic performance for CO combustion of the synthesized $La_{0.8}Sr_{0.2}Co_xFe_{1-x}O_{3-\delta}$ perovskites under oxidative and stoichiometric conditions is compared on the basis of the temperature required to obtain a r_{CO_2} equal to 10^{-7} mol s⁻¹ m⁻² (Figure 5a) and on the basis of the light-off temperature, T_{50} (Figure 5b). As shown in Figure 5a, the temperature corresponding to a CO₂ production rate of 10^{-7} mol s⁻¹ m⁻² decreased with increasing Co/Fe ratio under oxidative feed conditions over the entire range of Co/Fe ratios (LSF to LSC), whereas under stoichiometric feed conditions it decreased up to a Co/Fe ratio equal to 6/4, remaining practically the same for higher Co content. The same trend was observed concerning the T_{50} values (Figure 5b). Moreover,

with the exception of the less active LSF oxide, both the temperature corresponding to r_{CO_2} equal to $10^{-7} \text{ mol s}^{-1} \text{ m}^{-2}$ and T_{50} for each of the tested perovskites were lower under oxidative conditions compared to stoichiometric conditions, implying a higher catalytic performance in the former case. Considering the above observations, it can be concluded that the catalytic activity for CO oxidation, under both oxidative and stoichiometric feed conditions, depends strongly on the relative content of Co and Fe at the B-sites of the $\text{La}_{0.8}\text{Sr}_{0.2}\text{Co}_x\text{Fe}_{1-x}\text{O}_{3-\delta}$ perovskite oxides. Increasing the Co/Fe ratio results in an increase in the catalytic activity for CO combustion, more pronounced under oxidative reaction conditions. The lowest and highest activities among the tested materials were exhibited by the LSF and the LSC perovskites, respectively.

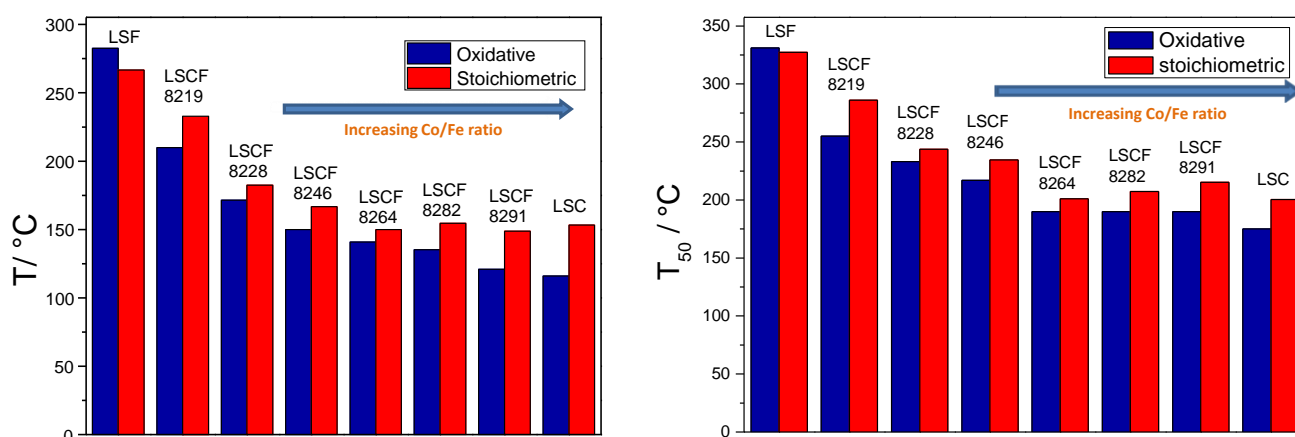


Figure 5. CO combustion on $\text{La}_{0.8}\text{Sr}_{0.2}\text{Co}_x\text{Fe}_{1-x}\text{O}_{3-\delta}$ perovskites under oxidative (1% CO/5% O_2 /balance He) and stoichiometric (1% CO/0.5% O_2 /balance He) feed conditions: (a) Temperatures corresponding to a CO_2 production rate of $10^{-7} \text{ mol s}^{-1} \text{ m}^{-2}$, measured under practically differential conditions and (b) light-off temperatures, T_{50} .

Kinetic measurements with varying O_2 partial pressures were conducted for the most active LSC catalyst, under practically differential conditions. Figure 6a shows, in the form of Arrhenius plot, the temperature dependence of the CO_2 production rate (r_{CO_2}), normalized to the SSA, for four different O_2 partial pressures P_{O_2} (0.5, 1, 2 and 5 kPa) and a constant CO partial pressure, P_{CO} , equal to 1 kPa. As expected, for all oxygen partial pressures, the CO_2 production rate increased exponentially with increasing temperature, whereas the apparent activation energy that was determined from the slopes of the Arrhenius plots ranged between $9.8 \text{ kcal mol}^{-1}$ for $P_{\text{O}_2} = 0.5 \text{ kPa}$ and $13.1 \text{ kcal mol}^{-1}$ for $P_{\text{O}_2} = 5 \text{ kPa}$. Moreover, at each temperature, r_{CO_2} was found to increase with increasing O_2 partial pressure, which implies a positive order of the reaction with respect to O_2 , in agreement with the higher activity observed under oxidative conditions compared to stoichiometric conditions (Figure 5). The latter behavior was observed for all tested perovskites; thus, it can be assumed that CO combustion is positive order with respect to O_2 on all of them.

The positive order of CO combustion with respect to O_2 is more clearly shown in Figure 6b, where is presented in the form of logarithmic plot the dependence of the CO_2 production rate on O_2 partial pressure at three different temperatures (115, 130, and 145°C), for constant CO partial pressure equal to 1 kPa. The slopes of the plots for the three temperatures do not differ significantly, corresponding to an apparent reaction order in oxygen of ca. 0.5.

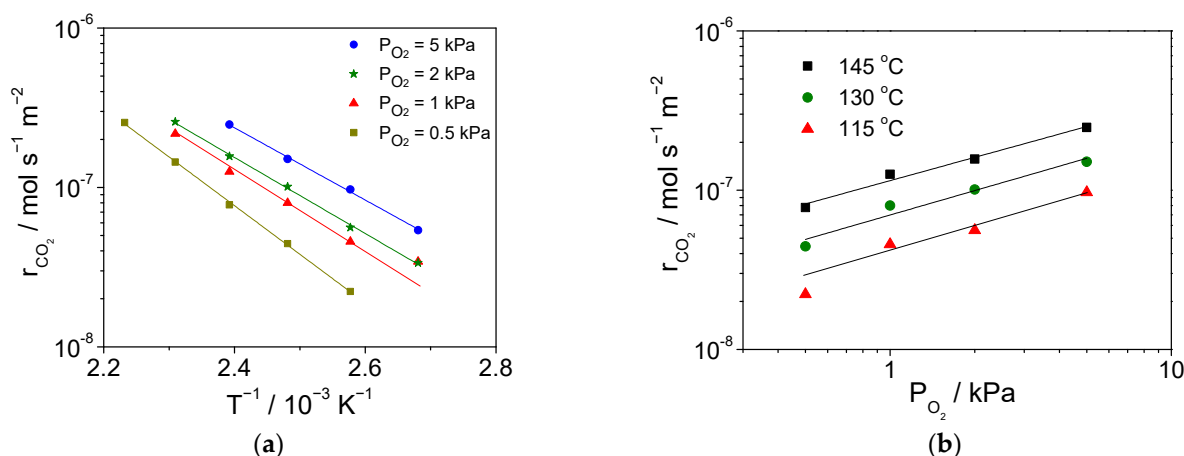


Figure 6. CO combustion on LSC. (a) Temperature dependence of the CO₂ production rate (Arrhenius plots) for four different O₂ partial pressures (P_{O_2} : 0.5, 1, 2 and 5 kPa) and $P_{CO} = 1$ kPa. (b) Effect of P_{O_2} on the CO₂ production rate, at constant $P_{CO} = 1$ kPa, for three different temperatures (115, 130, and 145 °C).

2.4. Catalytic Activity for Propane Combustion

The synthesized La_{0.8}Sr_{0.2}Co_xFe_{1-x}O_{3-δ} perovskites were also tested as catalysts for complete oxidation of propane under oxidative and stoichiometric conditions. Figure 7a shows, for all synthesized perovskites, the dependence of propane conversion ($X_{C_3H_8}$) on temperature, under oxidative feed conditions (0.5% C₃H₈/5% O₂/balance He). For all tested perovskite oxides, complete conversion of propane was achieved at temperatures ranging between 520 °C and 670 °C, which are higher than the corresponding ones for CO oxidation (Figure 3a). For the same temperature, increasing the Co/Fe ratio was accompanied by an increase in propane conversion, more pronounced for Co/Fe ratios up to 6/4 (Figure 7a). Equivalently, the light-off temperature (T_{50}) decreased with increasing Co/Fe ratio. Considering the above, it is concluded that the dependence of catalytic activity of La_{0.8}Sr_{0.2}Co_xFe_{1-x}O_{3-δ} perovskites on the Co/Fe ratio is similar for both CO and propane combustion, i.e., the activity is reduced with increasing Fe and decreasing Co content at the B-sites. The higher temperatures required for complete conversion of propane compared to CO (Figures 3a and 7a), under oxidative feed conditions, are expected since propane is a more complex molecule compared to CO.

Figure 7b,c present for all tested perovskites, in the form of Arrhenius plots, the temperature dependence of the CO₂ production rate (r_{CO_2}) in propane combustion under oxidative (0.5% C₃H₈/5% O₂/balance He) and stoichiometric (0.5% C₃H₈/2.5% O₂/balance He) feed conditions, respectively, with the rate being determined under practically differential conditions and normalized to SSA. As shown in Figure 7b, for oxidative conditions, with increasing Co content the same r_{CO_2} was obtained at lower temperature, more clearly for Co/Fe ≤ 6/4, which implies an increase in the catalytic activity for propane combustion. The temperature corresponding to a CO₂ production rate of 10⁻⁷ mol s⁻¹ m⁻² was equal to 345 °C and 244 °C for the less active (LSF) and the most active (LSC) perovskite catalysts, respectively. As shown in Figure 7c, practically the same behavior was observed for propane combustion under stoichiometric conditions, i.e., the same r_{CO_2} value was achieved at lower temperatures with increasing Co/Fe ratio, the effect being clearer for Co/Fe ratios up to 6/4. In this case, the temperature corresponding to a CO₂ production rate of 10⁻⁷ mol s⁻¹ m⁻² was 355 °C for the LSF and 255 °C for the LSC perovskites (Figure 7c). Also, the comparison of the data shown in Figure 7b,c reveals that the temperatures corresponding to a specific r_{CO_2} value, for example, 10⁻⁷ mol s⁻¹ m⁻², were lower under oxidative conditions compared to stoichiometric conditions for all the tested perovskites, which, similar to CO combustion, indicates a higher catalytic activity under oxidative conditions.

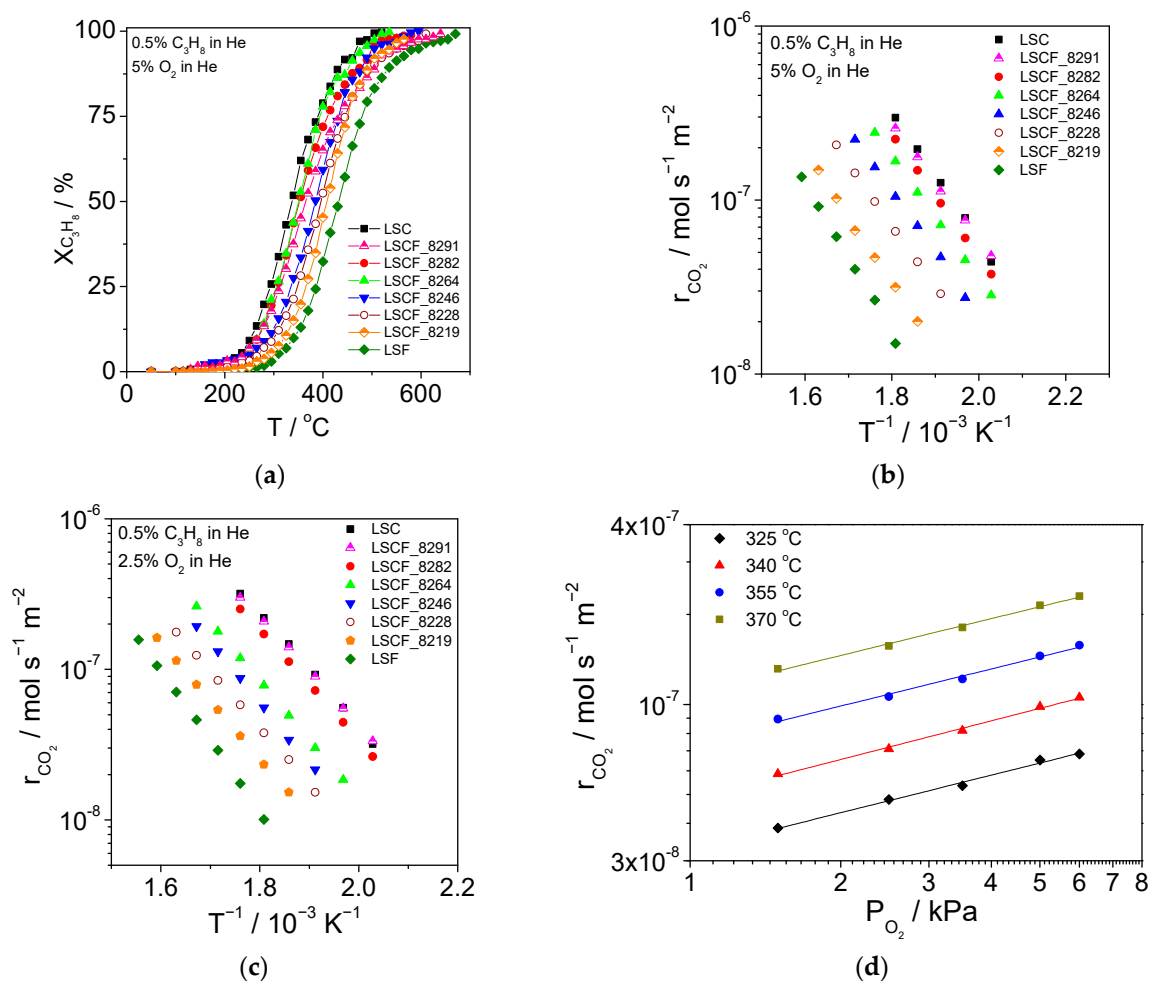


Figure 7. Propane combustion on $La_{0.8}Sr_{0.2}Co_xFe_{1-x}O_{3-\delta}$ perovskites: (a) C_3H_8 conversion as a function of temperature under oxidative feed conditions (0.5% C_3H_8 /5% O_2 /He), (b) temperature dependence of the CO_2 production rate under oxidative feed conditions (0.5% C_3H_8 /5% O_2 /balance He), (c) temperature dependence of the CO_2 production rate under stoichiometric feed conditions (0.5% C_3H_8 /2.5% O_2 /balance He), and (d) effect of oxygen partial pressure (P_{O_2}) on the CO_2 production rate, for the LSC catalyst, at constant propane partial pressure $P_{C_3H_8} = 0.5$ kPa and for four different temperatures (325 °C, 340 °C, 355 °C, and 370 °C).

Kinetic measurements were performed for propane combustion on the most active LSC perovskite. Figure 7d shows, in the form of logarithmic plots, the dependence of the CO_2 production rate on O_2 partial pressure at four different temperatures (325, 340, 355, and 370 °C), for constant propane partial pressure equal to 0.5 kPa. A positive order with respect to O_2 is observed, practically the same for all tested temperatures. This can explain the higher activity for propane combustion observed for LSC under oxidative conditions compared to stoichiometric conditions. As the same behavior was observed for the other tested perovskites, it can be assumed that also for them propane combustion is positive order with respect to O_2 (close to 0.5) in agreement with the observed higher activity under oxidative conditions.

3. Discussion

Oxygen adsorption on perovskites is a complex process, considered to occur mainly at the vicinity of B-sites of perovskite catalysts [13,59,60]. Adler et al. [61] assumed that two neighboring vacant surface lattice sites, similar to those in the bulk of the oxide, are involved in the dissociative adsorption of oxygen and surface oxygen exchange. Royer et al. in their review work [16] highlight the significant role of the oxidation state of the B-site

cations and of oxygen vacancies (created by partial substitution of the cations at the A- and/or B-sites) on the perovskite surface oxygen exchange and transport properties, which are also affected by the material microstructure. CO is chemisorbed molecularly on many transition metal oxides, via donation of electron density towards the metal cations, whereas the chemisorption of alkanes on transition metal oxides is generally dissociative [62]. Rhee and Lee [60] refer to two different adsorption states of CO on the surface of LaCoO_3 depending on temperature, namely, CO adsorbed in the form of carbonyl species on Co^{3+} cations at 167 °C and CO in the form of bidentate complexes with the lattice oxygen or/and with the surface adsorbed oxygen at 360 °C. It has also been reported that the main CO adsorption site on LaCoO_3 perovskite surface is provided by surface lattice oxygen, with formation of surface carbonate species [59,63]. Propane has been reported to adsorb dissociatively on unsubstituted and P-doped LaCoO_3 with the surface Co^{3+} sites acting as active sites for initial cleavage of a C-H bond and formation of an adsorbed alkyl radical [64]. Promotion of propane adsorption and dissociation has been also reported for LaCoO_3 perovskites with increased defect content, synthesized via a defect engineering route, being attributed to an increase in the number of Co^{3+} on the surface combined with an increase in lattice oxygen mobility and surface oxygen capacity, as also corroborated using DFT calculations [65]. Such calculations have been also used to study propane adsorption on macroporous $\text{La}_{0.8}\text{Sr}_{0.2}\text{CoO}_3$ perovskite oxides [66].

As mentioned in the Introduction section, two oxidation mechanisms are considered as dominant in $\text{AA}'\text{BB}'\text{O}_3$ perovskites, namely, the suprafacial mechanism, which involves only surface oxygen species, and the intrafacial mechanism, corresponding to a redox cycle involving surface lattice oxygen with possible participation of oxygen species originating from the bulk of the perovskite oxide, the prevailing reaction mechanism depending strongly on the perovskite composition and the reaction [12,14–16]. CO oxidation catalyzed by substituted $\text{AA}'\text{BO}_3$ and $\text{AA}'\text{BB}'\text{O}_3$ perovskites, with Co and Fe at the B and B'-sites, is considered to proceed via the intrafacial mechanism due to their higher ionic conductivity compared to other perovskites, associated mainly with their high lattice oxygen mobility [14]. This agrees with the observed high surface exchange in oxygen between the gas phase and the lattice structure of $\text{La}_{1-x}\text{Sr}_x\text{CoO}_3$ ($x: 0 - 0.6$) at low temperatures ($T < 300$ °C) [67] at which ABO_3 type perovskites tend to follow the suprafacial mechanism [14,15].

In the present study, a similar trend in the catalytic activity of $\text{La}_{0.8}\text{Sr}_{0.2}\text{Co}_x\text{Fe}_{1-x}\text{O}_{3-\delta}$ for both CO and propane combustion was observed as x varied from 0 (LSF) to 1 (LSC). This indicates that the intrafacial mechanism is probably prevailing, as in this case the rate determining step would be the surface lattice oxygen replenishment for both reactions. The prevalence of the intrafacial mechanism is also corroborated by the fact that, as mentioned above, the tested perovskites exhibit a higher number of oxygen ion vacancies, an improved reducibility of the B-site ions, and a higher surface oxygen exchange as well as a higher mobility of oxygen ions compared to LaFeO_3 and LaCoO_3 [5,12,14,44,58,67] for which a suprafacial mechanism for CO oxidation at temperatures below 350 °C has been suggested [5,12,14,15]. In this respect, the observed increase in catalytic activity with increasing substitution of iron by cobalt at the B-sites can be mainly attributed to the induced change in the number of lattice oxygen vacancies associated with the easier alteration of the redox state of the Co cations compared to Fe cations [56–58], which increases lattice oxygen anion mobility and enhances surface oxygen exchange [14,54,58], thus favoring the aforementioned redox cycle corresponding to the intrafacial mechanism. The easier release of oxygen from the perovskite oxides with increasing Co/Fe ratio (from LSF to LSC) is corroborated by the observed shift in the onset reduction temperature to lower values in the H_2 -TRP profiles (Figure 2). The preferential release of oxygen from oxygen sites in the vicinity of Co rather than Fe sites, as a result of the easier reduction of Co cations compared to Fe cations, has also been observed by Itoh et al. [68] for $\text{La}_{0.6}\text{Sr}_{0.4}\text{Co}_{0.2}\text{Fe}_{0.8}\text{O}_{3-\delta}$ using in situ X-ray absorption spectroscopy. The increase in oxygen non-stoichiometry, or equivalently in the number of oxygen vacancies, induced by substitution of Fe by Co at the

B-sites of $\text{La}_{1-x}\text{Sr}_x\text{Co}_{1-y}\text{Fe}_y\text{O}_{3-\delta}$ perovskites has been demonstrated by Scott et al. [27] using solid electrolyte coulometry and CO-TPR measurements. Similarly, Lankhorst and ten Elshof [28] using coulometric titration at 650–950 °C reported a decrease in the oxygen non-stoichiometry in $\text{La}_{0.6}\text{Sr}_{0.4}\text{Co}_{1-y}\text{Fe}_y\text{O}_{3-\delta}$ with increasing Fe content at the B-sites (changing y from 0 to 0.6), which they associated with an increase in the O^{2-} binding energy in the lattice and with the preferential formation of holes over oxygen vacancies.

The results of the present study are in agreement with the reported by Levasseur and Kaliaguine [29] decrease in the catalytic activity of $\text{La}_{1-y}\text{Ce}_y\text{Co}_{1-x}\text{Fe}_x\text{O}_3$ for CO combustion with partial substitution of Co by Fe at the B-sites, which they attributed to a decrease in the reducibility of the B-site cations and in the mobility of oxygen in the perovskite bulk. These results also agree with the observed by Tanaka et al. [30] increase in the catalytic activity for propane combustion of $\text{La}_{0.9}\text{Ce}_{0.1}\text{Co}_{1-x}\text{Fe}_x\text{O}_3$ (x : 0 to 1) with increasing Co content and with the reported by Merino et al. [45] increase in the catalytic activity of $\text{LaCo}_{1-y}\text{Fe}_y\text{O}_{3\pm\lambda}$ ($y = 0.1, 0.5, 1$) for the same reaction with decreasing y (partial substitution of Fe by Co).

It is noted that the observed variation in catalytic activity of the tested perovskites for CO and propane combustion with changing Fe/Co ratio could be also attributed, to a lesser extent, to the observed changes in their structural characteristics (Section 2.1), which are associated with the surface electronic structure and, thus, may affect the chemisorptive bond strengths of the reactants [16,31,48,50].

4. Materials and Methods

4.1. Synthesis of the Perovskite Oxides

The synthesis method of the perovskite oxides affects significantly their physical properties, including particle size, porosity, and specific surface area (SSA). Synthesis of a perovskite material with high SSA and porosity is expected to enhance its catalytic or electrocatalytic performance. Therefore, the perovskite synthesis methods reported in the literature focus on fine-tuning of the aforementioned physical properties for specific applications [69]. In the present work, the in situ combustion method, with citric acid as fuel, was applied for synthesis of the tested $\text{La}_{0.8}\text{Sr}_{0.2}\text{Co}_x\text{Fe}_{1-x}\text{O}_{3-\delta}$ perovskites, as described in detail in a previous study of our group [47].

The following metal nitrates, in the form of solutions in triple-distilled water, were used as metal precursors: $\text{La}(\text{NO}_3)_3 \cdot 6\text{H}_2\text{O}$ (99.9% REO, Alfa Aesar, Karlsruhe, Germany), $\text{Sr}(\text{NO}_3)_2$ (99+%, ACS reagent, Sigma-Aldrich Chemie, Steinheim, Germany), $\text{Fe}(\text{NO}_3)_3 \cdot 9\text{H}_2\text{O}$ ($\geq 99.0\%$, Merck, Darmstadt, Germany), and $\text{Co}(\text{NO}_3)_2 \cdot 6\text{H}_2\text{O}$ ($\geq 99.0\%$ KT, ACS reagent, Sigma-Aldrich Chemie, Steinheim, Germany). Citric acid monohydrate ($\text{C}_6\text{H}_8\text{O}_7 \cdot \text{H}_2\text{O}$, 99.5–100.5% assay, Merck, Darmstadt, Germany) and ammonium nitrate (NH_4NO_3 , $\geq 99.0\%$, Sigma-Aldrich, St. Louis, MO, USA) were used as fuel and extra oxidant, respectively [47]. Citric acid was diluted in triple-distilled water to form a 1.7 M solution, and an appropriate amount of this solution was added under continuous stirring to the metal precursors solution to obtain a citric acid-to-metal ions molar ratio equal to 2:1 [47,70]. An amount of NH_4NO_3 was also added to obtain a molar ratio of NH_4NO_3 -to-metal ions equal to 1:1 [47]. The presence of ammonium nitrate, which does not affect the chemical composition of the synthesized perovskite, both accelerates the combustion, reducing sintering time after the formation of the perovskite, and yields in the production of extra amount of gasses that have a dilatative effect on the microstructure of the material, which results in an increase in the SSA of the oxide [71]. An appropriate amount of ammonia solution (30 wt.%, Carlo Erba) was then added dropwise until reaching a pH value of ca. 9 [47,70] in order to neutralize the excess citric acid and form a colloidal solution (sol) [72]. This solution was heated under magnetic stirring on a hot plate until evaporation of H_2O . The resulting slurry was then heated up to ca. 400 °C, using a heat gun, in order to initiate ignition and form a thin crust. The powder, which resulted from shattering the crust, was calcined at 900 °C for 5 h in stagnant air to form the crystalline perovskite phase, and, finally, was finely grounded in a mortar [47].

4.2. Physicochemical Characterization of the Perovskite Oxides (BET, XRD, and ICP-OES)

The specific surface areas (SSAs) of the synthesized perovskite powders were determined via nitrogen physisorption at liquid N₂ temperature (BET method), using a TriStar 3000 surface area and porosimetry analyzer (Micromeritics, Norcross, GA, USA) preceded by degassing of the perovskite samples under vacuum at 300 °C for 1 h [47].

X-ray diffraction (XRD) measurements were performed in order to determine the structural characteristics of the synthesized perovskite materials. XRD spectra were obtained for 2 θ values ranging from 10° to 90° at a rate of 0.04 ° s⁻¹, using a Bruker AXS D8 Advance diffractometer, which was equipped with a Cu-K α lamp (λ = 1.54062 Å) and a Ni filter [47]. The identification and analysis of the observed phases were performed using the EVA software (Bruker AXS, Karlsruhe, Germany).

After previous acid digestion of the perovskite powders, their exact stoichiometry was determined with inductively coupled plasma optical emission spectroscopy (ICP-OES) in an Optima 7000 DV ICP-OES system (Perkin Elmer, Waltham, MA, USA) [47].

4.3. H₂ Temperature-Programmed Reduction Characterization

H₂ temperature-programmed reduction measurements were performed in order to assess and compare the reducibility of the synthesized perovskites. The apparatus used for the experiments consisted of a gas flow system, a quartz reactor positioned in an open-ended vertical electric furnace, and an Omnistar™ GSD301 O1 quadrupole mass spectrometer (Pfeiffer Vacuum, Asslar, Germany) interfaced to a personal computer for on-line monitoring of the TPR effluent gas, using the Quadstar 32-bit (version 7.03) software (Pfeiffer Vacuum, Asslar, Germany). The perovskite mass used in each experiment was 150 mg. The sample was placed in the reactor in the form of a fixed bed deposited on quartz wool and was initially heat treated under He flow at 500 °C for 15 min to remove any adsorbed species [73]. Heat treatment continued under flow of 21% O₂/He mixture at the same temperature for 30 min, followed by free cooling to room temperature (ca. 25 °C). Then, the feed was sequentially switched to He for 15 min and to 3.9% H₂/He mixture for 10 min. Afterwards, the TPR experiment was started by linearly increasing the temperature of the sample up to 720 °C at a rate of 30 °C min⁻¹, using a Eurotherm 815 controller/programmer, and simultaneously monitoring hydrogen in the reactor effluent by recording the transient mass spectrometer signal at mass-to-charge ratio m/z = 2. The temperature of the sample was measured by means of a type-K thermocouple. The gas feed flow rate was equal to 30 cm³ min⁻¹ in all the above steps.

4.4. Catalytic Oxidation Measurements

The experimental apparatus used for the CO and propane combustion measurements consisted of a fixed-bed quartz tube reactor positioned in an open-ended vertical electric furnace, a gas flow system, and an analysis system. The composition and flow rate of the gas mixture fed to the reactor in down-flow mode were adjusted using three electronic mass flow controllers (Aera FC-7700C connected to a ROD-4 operating unit, Advanced Energy Industries, Inc., Fort Collins, CO, USA). Reaction gases were high purity O₂/He, CO or C₃H₈/He mixtures, and He. The perovskite powder (120 mg) was placed on quartz wool in the middle of the quartz tube reactor (8 mm internal diameter). The temperature of the perovskite catalyst was measured in the middle of the catalyst bed using a K-type thermocouple enclosed in a quartz tube entering the upper part of the reactor through a tee connection and was controlled using a Eurotherm 2216e temperature controller. The analysis system consisted of a non-dispersive infrared CO–CO₂ analyzer (BINOS® 100, Rosemount Analytical/Emerson Process Management, Hasselroth, Germany), for continuous monitoring of CO and CO₂ concentration, and a gas chromatograph (TRACE™ CG Ultra, Thermo Fischer Scientific, Inc., Waltham, MA, USA) equipped with a thermal conductivity detector (TCD) and a 6-port sampling valve (VICI Valco). A Carbosieve SII 80/100 (1.8" O.D. × 8 ft) stainless steel packed column operating at 120 °C was used for analysis of the reaction mixture in CO combustion, whereas a cascade of a 23% SP®-1700

on 80/100 Chromosorb P AW (1.8"O.D. × 8 ft) and a 10% TCEP on 100/120 Chromosorb P AW (1.8"O.D. × 8 ft) stainless steel packed columns, operating at 40 °C, were used for analysis of the reaction mixture in propane combustion, using He as carrier gas in both cases. Analysis of the reactor feed was possible by bypassing the reactor using a 4-port valve (VICI Valco). The experiments were carried out under practically atmospheric pressure in the temperature range 50–670 °C, using a total feed flow rate of 100 cm³ min⁻¹. For this flow rate, the pressure drop across the catalyst fixed-bed reactor, as measured using a manometer, was negligible (less than 0.01 atm). The gas hourly space velocity (GHSV) was equal to 27,500 h⁻¹, as calculated using a measured bulk catalyst bed density value of 0.55 g cm⁻³. Oxidative (1% CO–5% O₂ and 0.5% C₃H₈–5% O₂) and stoichiometric (1% CO–0.5% O₂ and 0.5% C₃H₈–2.5% O₂) feed compositions were used, with He as balance gas. All measurements were performed after previous establishment of steady-state conditions. No indication of catalyst deactivation due to the produced H₂O(g) was observed during the catalytic measurements concerning propane combustion.

5. Conclusions

In the present work, a series of eight La_{0.8}Sr_{0.2}Co_xFe_{1-x}O_{3-δ} perovskites, with x = 0, 0.1, 0.2, 0.4, 0.6, 0.8, 0.9, and 1, were synthesized via the in situ combustion synthesis method, and their catalytic activities for CO and C₃H₈ combustion were compared. The perovskite powders were characterized with respect to their specific surface area (SSA), structure, and reducibility via N₂ physisorption (BET method), XRD, and H₂-TPR, respectively, while their chemical composition was determined via ICP-OES.

Their SSA values ranged between 4.1 (La_{0.8}Sr_{0.2}Co_{0.9}Fe_{0.1}O_{3-δ}) and 7.9 m² g⁻¹ (La_{0.8}Sr_{0.2}Co_{0.1}Fe_{0.9}O_{3-δ}). XRD confirmed the formation of the perovskite structure for all synthesized materials and the absence of secondary phases. A shift in the XRD peaks to higher 2θ was observed with increasing partial substitution of Fe by Co at the B-sites, indicating a contraction of the perovskite unit cell. This shift was accompanied by a gradual change in the main peak (located at 2θ between 32 and 33°) from single to doublet, implying a change in the perovskite symmetry from orthorhombic to rhombohedral.

The H₂-TPR profiles of all synthesized perovskites were characterized by the presence of a broad main reduction peak that can be attributed to the reaction of hydrogen with surface oxygen partly replenished by lattice oxygen migrating from the oxide bulk as the temperature increased. The onset temperature of the reduction process was shifted towards lower values with increasing Co/Fe ratio accompanied by an increase in the main reduction peak, clearly for Co/Fe ≤ 6/4. This indicates an easier release of the surface lattice oxygen species and an easier transport of oxygen from the oxide bulk with increasing Co/Fe ratio, which can be mainly associated with the more facile change in the oxidation state of the cobalt cations compared to iron cations.

The catalytic performance of the synthesized La_{0.8}Sr_{0.2}Co_xFe_{1-x}O_{3-δ} perovskites for CO and propane combustion was investigated in a fixed bed reactor under oxidative and stoichiometric feed conditions. Increase in the Co/Fe ratio, from La_{0.8}Sr_{0.2}FeO_{3-δ} (LSF) to La_{0.8}Sr_{0.2}CoO_{3-δ} (LSC), resulted in an enhancement of the catalytic activity for both CO and propane combustion, as concluded both from conversion vs. temperature curves and from CO₂ production rate measurements under practically differential conditions. For CO combustion, the effect of changing the relative content of Co and Fe at the B-sites on catalytic activity was more pronounced under oxidative feed conditions (1% CO/5% O₂/balance He), whereas under stoichiometric feed conditions (1% CO/0.5% O₂/balance He) it was more significant for Co/Fe ≤ 6/4. A higher activity of the tested catalytic materials was observed under oxidative reaction conditions compared to stoichiometric conditions, which can be attributed to positive order kinetics with respect to oxygen. The latter was confirmed with kinetic measurements performed for both CO and propane oxidation using La_{0.8}Sr_{0.2}CoO_{3-δ} as catalyst.

The observed enhancement of the catalytic activity of La_{0.8}Sr_{0.2}Co_xFe_{1-x}O_{3-δ} perovskites for CO and propane combustion with increasing Co/Fe ratio can be mainly

explained on the basis of a prevailing redox catalytic cycle (intrafacial mechanism), considering that the increase in the Co content at the expense of iron induces an increase in the number of catalytically active sites, as they are related to oxygen vacancies at the vicinity of the Co B-sites, and enhances oxygen surface exchange kinetics, due to the lower redox stability of cobalt cations compared iron cations, as also corroborated by the results of the H₂-TPR experiments.

Author Contributions: Conceptualization, A.S., V.C.K. and S.B.; methodology, A.S., V.C.K. and S.B.; investigation, A.S., V.C.K., G.B. and S.B.; visualization; A.S., V.C.K. and G.B.; writing—original draft preparation, A.S., G.B. and S.B.; writing—review and editing, G.B. and S.B.; resources, S.B.; supervision, S.B.; project administration; S.B. All authors have read and agreed to the published version of the manuscript.

Funding: This research received no external funding.

Data Availability Statement: Any data not presented in the manuscript are available upon reasonable written request from the corresponding author.

Acknowledgments: The assistance of Vassilios Dracopoulos, FORTH/ICE-HT, with the XRD characterization and Dimitra Kanellopoulou with the ICP-OES characterization of the perovskite powders is gratefully acknowledged. We also appreciate the permission of D. I. Kondarides to use the TPR apparatus in the Laboratory of Heterogeneous Catalysis of our Department.

Conflicts of Interest: The authors declare no conflict of interest.

References

1. Dey, S.; Sun, S.; Mehta, N.S. Carbon monoxide catalytic oxidation over various iron-based nanoparticles at ambient conditions: A Review. *Carbon Capture Sci. Technol.* **2021**, *1*, 100013. [[CrossRef](#)]
2. Yuan, C.; Wu, H.B.; Xie, Y.; Lou, X.W. Mixed transition-metal oxides: Design, synthesis, and energy-related applications. *Angew. Chem. Int. Ed.* **2014**, *53*, 1488–1504. [[CrossRef](#)]
3. Huang, W. Oxide Nanocrystal Model Catalysts. *Acc. Chem. Res.* **2016**, *49*, 520–527. [[CrossRef](#)] [[PubMed](#)]
4. Yakoumis, I.; Panou, M.; Moschovi, A.M.; Pania, D. Recovery of platinum group metals from spent automotive catalysts: A review. *Clean. Eng. Technol.* **2021**, *3*, 100112. [[CrossRef](#)]
5. Laguna, O.H.; Bobadilla, L.F.; Hernández, W.Y.; Centeno, M.A. Low-Temperature CO Oxidation. In *Perovskites and Related Mixed Oxides: Concepts and Applications*; Granger, P., Parvulescu, V.I., Kaliaguine, S., Prellier, W., Eds.; Wiley-VCH Verlag GmbH & Co. KGaA: Weinheim, Germany, 2016; pp. 451–473. [[CrossRef](#)]
6. Pramuanjaroenkij, A.; Kakaç, S. The fuel cell electric vehicles: The highlight review. *Int. J. Hydrogen Energy* **2023**, *48*, 9401–9425. [[CrossRef](#)]
7. Jiao, K.; Xuan, J.; Du, Q.; Bao, Z.; Xie, B.; Wang, B.; Zhao, Y.; Fan, L.; Wang, H.; Hou, Z.; et al. Designing the next generation of proton-exchange membrane fuel cells. *Nature* **2021**, *595*, 361–369. [[CrossRef](#)]
8. Bampos, G.; Bebelis, S. Performance of a Pd-Zn Cathode Electrode in a H₂ Fueled Single PEM Fuel Cell. *Electronics* **2022**, *11*, 2776. [[CrossRef](#)]
9. Liu, H.; Li, D.; Guo, J.; Li, Y.; Liu, A.; Bai, Y.; He, D. Recent advances on catalysts for preferential oxidation of CO. *Nano Res.* **2022**, *16*, 4399–4410. [[CrossRef](#)]
10. Feng, C.; Liu, X.; Zhu, T.; Tian, M. Catalytic oxidation of CO on noble metal-based catalysts. *Environ. Sci. Pollut. Res. Int.* **2021**, *28*, 24847–24871. [[CrossRef](#)]
11. Prasad, R.; Singh, P. A Review on CO Oxidation Over Copper Chromite Catalyst. *Catal. Rev.* **2012**, *54*, 224–279. [[CrossRef](#)]
12. Royer, S.; Duprez, D. Catalytic Oxidation of Carbon Monoxide over Transition Metal Oxides. *ChemCatChem* **2011**, *3*, 24–65. [[CrossRef](#)]
13. Peña, M.A.; Fierro, J.L.G. Chemical Structures and Performance of Perovskite Oxides. *Chem. Rev.* **2001**, *101*, 1981–2018. [[CrossRef](#)] [[PubMed](#)]
14. Yamazoe, N.; Teraoka, Y. Oxidation catalysis of perovskites—relationships to bulk structure and composition (valency, defect, etc.). *Catal. Today* **1990**, *8*, 175–199. [[CrossRef](#)]
15. Voorhoeve, R.J.H. Perovskite-Related Oxides as Oxidation—Reduction Catalysts. In *Advanced Materials in Catalysis*; Burton, J.J., Garten, R.L., Eds.; Academic Press, Inc.: New York, NY, USA, 1977; pp. 129–180. [[CrossRef](#)]
16. Royer, S.; Duprez, D.; Can, F.; Courtois, X.; Batiot-Dupeyrat, C.; Laassiri, S.; Alamdari, H. Perovskites as Substitutes of Noble Metals for Heterogeneous Catalysis: Dream or Reality. *Chem. Rev.* **2014**, *114*, 10292–10368. [[CrossRef](#)]

17. Giordano, L.; Akkiraju, K.; Jacobs, R.; Vivona, D.; Morgan, D.; Shao-Horn, Y. Electronic Structure-Based Descriptors for Oxide Properties and Functions. *Acc. Chem. Res.* **2022**, *55*, 298–308. [[CrossRef](#)]
18. Yang, C.; Grimaud, A. Factors Controlling the Redox Activity of Oxygen in Perovskites: From Theory to Application for Catalytic Reactions. *Catalysts* **2017**, *7*, 149. [[CrossRef](#)]
19. Polo-Garzon, F.; Wu, Z. Acid–base catalysis over perovskites: A review. *J. Mater. Chem. A* **2018**, *6*, 2877–2894. [[CrossRef](#)]
20. Zhu, H.; Zhang, P.; Dai, S. Recent Advances of Lanthanum-Based Perovskite Oxides for Catalysis. *ACS Catal.* **2015**, *5*, 6370–6385. [[CrossRef](#)]
21. Wang, T.; Zhang, C.; Wang, J.; Li, H.; Duan, Y.; Liu, Z.; Lee, J.Y.; Hu, X.; Xi, S.; Du, Y.; et al. The interplay between the suprafacial and intrafacial mechanisms for complete methane oxidation on substituted LaCoO₃ perovskite oxides. *J. Catal.* **2020**, *390*, 1–11. [[CrossRef](#)]
22. Mars, P.; van Krevelen, D.W. Oxidations carried out by means of vanadium oxide catalysts. *Chem. Eng. Sci.* **1954**, *3*, 41–59. [[CrossRef](#)]
23. Pecchi, G.; Jiliberto, M.G.; Buljan, A.; Delgado, E.J. Relation between defects and catalytic activity of calcium doped LaFeO₃ perovskite. *Solid State Ion.* **2011**, *187*, 27–32. [[CrossRef](#)]
24. Kizaki, H.; Kusakabe, K. *Ab-initio* study of Sr-doping effects on nitric oxide adsorption on the LaO (001) surface of LaFeO₃. *Surf. Sci.* **2012**, *606*, 1783–1789. [[CrossRef](#)]
25. Merino, N.A.; Barbero, B.P.; Grange, P.; Cadús, L.E. La_{1-x}Ca_xCoO₃ perovskite-type oxides: Preparation, characterisation, stability, and catalytic potentiality for the total oxidation of propane. *J. Catal.* **2005**, *231*, 232–244. [[CrossRef](#)]
26. Zhang, H.M.; Shimizu, Y.; Teraoka, Y.; Miura, N.; Yamazoe, N. Oxygen sorption and catalytic properties of La_{1-x}Sr_xCo_{1-y}Fe_yO₃ perovskite-type oxides. *J. Catal.* **1990**, *121*, 432–440. [[CrossRef](#)]
27. Scott, S.P.; Mantzavinos, D.; Hartley, A.; Sahibzada, M.; Metcalfe, I.S. Reactivity of LSCF perovskites. *Solid State Ion.* **2002**, *152–153*, 777–781. [[CrossRef](#)]
28. Lankhorst, M.H.R.; ten Elshof, J.E. Thermodynamic Quantities and Defect Structure of La_{0.6}Sr_{0.4}Co_{1-y}Fe_yO_{3-δ} (y=0–0.6) from High-Temperature Coulometric Titration Experiments. *J. Solid State Chem.* **1997**, *130*, 302–310. [[CrossRef](#)]
29. Levasseur, B.; Kaliaguine, S. Effects of iron and cerium in La_{1-y}Ce_yCo_{1-x}Fe_xO₃ perovskites as catalysts for VOC oxidation. *Appl. Catal. B Environ.* **2009**, *88*, 305–314. [[CrossRef](#)]
30. Tanaka, H.; Mizuno, N.; Misono, M. Catalytic activity and structural stability of La_{0.9}Ce_{0.1}Co_{1-x}Fe_xO₃ perovskite catalysts for automotive emissions control. *Appl. Catal. A Gen.* **2003**, *244*, 371–382. [[CrossRef](#)]
31. Isupova, L.A.; Sadykov, V.A.; Tsybulya, S.V.; Kryukova, G.N.; Ivanov, V.P.; Petrov, A.N.; Kononchuk, O.F. Effect of structural disorder on the catalytic activity of mixed La–Sr–Co–Fe–O perovskites. *React. Kinet. Catal. Lett.* **1997**, *62*, 129–135. [[CrossRef](#)]
32. David, E.; Niculescu, V.-C. Volatile Organic Compounds (VOCs) as Environmental Pollutants: Occurrence and Mitigation Using Nanomaterials. *Int. J. Environ. Res. Public Health* **2021**, *18*, 13147. [[CrossRef](#)]
33. Avila, M.S.; Vignatti, C.I.; Apesteguía, C.R.; Garetto, T.F. Effect of support on the deep oxidation of propane and propylene on Pt-based catalysts. *Chem. Eng. J.* **2014**, *241*, 52–59. [[CrossRef](#)]
34. Luo, Y.; Zuo, J.; Feng, X.; Qian, Q.; Zheng, Y.; Lin, D.; Huang, B.; Chen, Q. Good interaction between well dispersed Pt and LaCoO₃ nanorods achieved rapid Co³⁺/Co²⁺ redox cycle for total propane oxidation. *Chem. Eng. J.* **2019**, *357*, 395–403. [[CrossRef](#)]
35. O'Brien, C.P.; Jenness, G.R.; Dong, H.; Vlachos, D.G.; Lee, I.C. Deactivation of Pt/Al₂O₃ during propane oxidation at low temperatures: Kinetic regimes and platinum oxide formation. *J. Catal.* **2016**, *337*, 122–132. [[CrossRef](#)]
36. Hu, Z.; Wang, Z.; Guo, Y.; Wang, L.; Guo, Y.; Zhang, J.; Zhan, W. Total Oxidation of Propane over a Ru/CeO₂ Catalyst at Low Temperature. *Environ. Sci. Technol.* **2018**, *52*, 9531–9541. [[CrossRef](#)] [[PubMed](#)]
37. Hu, Z.; Liu, X.; Meng, D.; Guo, Y.; Guo, Y.; Lu, G. Effect of Ceria Crystal Plane on the Physicochemical and Catalytic Properties of Pd/Ceria for CO and Propane Oxidation. *ACS Catal.* **2016**, *6*, 2265–2279. [[CrossRef](#)]
38. Wang, W.; Li, D.; Yu, H.; Liu, C.; Tang, C.; Chen, J.; Lu, J.; Luo, M. Insights into Different Reaction Behaviors of Propane and CO Oxidation over Pt/CeO₂ and Pt/Nb₂O₅: The Crucial Roles of Support Properties. *J. Phys. Chem. C* **2021**, *125*, 19301–19310. [[CrossRef](#)]
39. Ma, L.; Geng, Y.; Chen, X.; Yan, N.; Li, J.; Schwank, J.W. Reaction mechanism of propane oxidation over Co₃O₄ nanorods as rivals of platinum catalysts. *Chem. Eng. J.* **2020**, *402*, 125911. [[CrossRef](#)]
40. Klvana, D.; Song, K.S.; Kirchnerova, J. Catalytic performance of La_{0.66}Sr_{0.34}Co_{0.2}Fe_{0.8}O₃ perovskite in propane combustion: Effect of preparation and specific surface area. *Korean J. Chem. Eng.* **2002**, *19*, 932–939. [[CrossRef](#)]
41. Vannice, M.A. An analysis of the Mars–van Krevelen rate expression. *Catal. Today* **2007**, *123*, 18–22. [[CrossRef](#)]
42. Alifanti, M.; Kirchnerova, J.; Delmon, B.; Klvana, D. Methane and propane combustion over lanthanum transition-metal perovskites: Role of oxygen mobility. *Appl. Catal. A Gen.* **2004**, *262*, 167–176. [[CrossRef](#)]
43. Nakamura, T.; Misono, M.; Yoneda, Y. Reduction-oxidation and catalytic properties of La_{1-x}Sr_xCoO₃. *J. Catal.* **1983**, *83*, 151–159. [[CrossRef](#)]
44. Nitadori, T.; Misono, M. Catalytic properties of La_{1-x}A'_xFeO₃ (A' = Sr,Ce) and La_{1-x}Ce_xCoO₃. *J. Catal.* **1985**, *93*, 459–466. [[CrossRef](#)]

45. Merino, N.A.; Barbero, B.P.; Ruiz, P.; Cadús, L.E. Synthesis, characterisation, catalytic activity and structural stability of $\text{LaCo}_{1-y}\text{Fe}_y\text{O}_{3\pm\lambda}$ perovskite catalysts for combustion of ethanol and propane. *J. Catal.* **2006**, *240*, 245–257. [[CrossRef](#)]
46. Song, K.S.; Klvana, D.; Kirchnerova, J. Kinetics of propane combustion over $\text{La}_{0.66}\text{Sr}_{0.34}\text{Ni}_{0.3}\text{Co}_{0.7}\text{O}_3$ perovskite. *Appl. Catal. A Gen.* **2001**, *213*, 113–121. [[CrossRef](#)]
47. Safakas, A.; Bampos, G.; Bebelis, S. Oxygen reduction reaction on $\text{La}_{0.8}\text{Sr}_{0.2}\text{Co}_x\text{Fe}_{1-x}\text{O}_{3-\delta}$ perovskite/carbon black electrocatalysts in alkaline medium. *Appl. Catal. B Environ.* **2019**, *244*, 225–232. [[CrossRef](#)]
48. Natile, M.M.; Poletto, F.; Galenda, A.; Glisenti, A.; Montini, T.; De Rogatis, L.; Fornasiero, P. $\text{La}_{0.6}\text{Sr}_{0.4}\text{Co}_{1-y}\text{Fe}_y\text{O}_{3-\delta}$ Perovskites: Influence of the Co/Fe Atomic Ratio on Properties and Catalytic Activity toward Alcohol Steam-Reforming. *Chem. Mater.* **2008**, *20*, 2314–2327. [[CrossRef](#)]
49. Tai, L.-W.; Nasrallah, M.M.; Anderson, H.U.; Sparlin, D.M.; Sehlin, S.R. Structure and electrical properties of $\text{La}_{1-x}\text{Sr}_x\text{Co}_{1-y}\text{Fe}_y\text{O}_3$. Part 1. The system $\text{La}_{0.8}\text{Sr}_{0.2}\text{Co}_{1-y}\text{Fe}_y\text{O}_3$. *Solid State Ion.* **1995**, *76*, 259–271. [[CrossRef](#)]
50. Gholizadeh, A. The effects of A/B-site substitution on structural, redox and catalytic properties of lanthanum ferrite nanoparticles. *J. Mater. Res. Technol.* **2019**, *8*, 457–466. [[CrossRef](#)]
51. Cullity, B.D.; Stock, S.R. *Elements of X-ray Diffraction*, 3rd ed.; Pearson Education, Ltd.: Harlow, UK, 2001; p. 174.
52. Mote, V.D.; Purushotham, Y.; Dole, B.N. Williamson-Hall analysis in estimation of lattice strain in nanometer-sized ZnO particles. *J. Theor. Appl. Phys.* **2012**, *6*, 6. [[CrossRef](#)]
53. Bampos, G.; Sygellou, L.; Bebelis, S. Oxygen reduction reaction activity of Pd-based bimetallic electrocatalysts in alkaline medium. *Catal. Today* **2020**, *355*, 685–697. [[CrossRef](#)]
54. Deng, J.; Dai, H.; Jiang, H.; Zhang, L.; Wang, G.; He, H.; Au, C.T. Hydrothermal Fabrication and Catalytic Properties of $\text{La}_{1-x}\text{Sr}_x\text{M}_{1-y}\text{Fe}_y\text{O}_3$ (M = Mn, Co) That Are Highly Active for the Removal of Toluene. *Environ. Sci. Technol.* **2010**, *44*, 2618–2623. [[CrossRef](#)] [[PubMed](#)]
55. García-López, E.; Marci, G.; Puleo, F.; La Parola, V.; Liotta, L.F. $\text{La}_{1-x}\text{Sr}_x\text{Co}_{1-y}\text{Fe}_y\text{O}_{3-\delta}$ perovskites: Preparation, characterization and solar photocatalytic activity. *Appl. Catal. B Environ.* **2015**, *178*, 218–225. [[CrossRef](#)]
56. Kuhn, J.N.; Ozkan, U.S. Effect of Co Content Upon the Bulk Structure of Sr- and Co-doped LaFeO_3 . *Catal. Lett.* **2008**, *121*, 179–188. [[CrossRef](#)]
57. Siebert, E.; Roux, C.; Boréave, A.; Gaillard, F.; Vernoux, P. Oxido-reduction properties of $\text{La}_{0.75}\text{Sr}_{0.3}\text{Co}_{0.8}\text{Fe}_{0.2}\text{O}_{3-\delta}$ perovskite oxide catalyst. *Solid State Ion.* **2011**, *183*, 40–47. [[CrossRef](#)]
58. Chang, H.; Bjørgum, E.; Mihai, O.; Yang, J.; Lein, H.L.; Grande, T.; Raaen, S.; Zhu, Y.-A.; Holmen, A.; Chen, D. Effects of Oxygen Mobility in La-Fe-Based Perovskites on the Catalytic Activity and Selectivity of Methane Oxidation. *ACS Catal.* **2020**, *10*, 3707–3719. [[CrossRef](#)]
59. Tascón, J.M.D.; García Fierro, J.L.; González Tejuca, L. Kinetics and Mechanism of CO Oxidation on LaCoO_3 . *Z. Phys. Chem.* **1981**, *124*, 249–257. [[CrossRef](#)]
60. Rhee, C.K.; Lee, H.-I. CO oxidation on LaCoO_3 perovskite. *Korean J. Chem. Eng.* **1994**, *11*, 48–54. [[CrossRef](#)]
61. Adler, S.B.; Chen, X.Y.; Wilson, J.R. Mechanisms and rate laws for oxygen exchange on mixed-conducting oxide surfaces. *J. Catal.* **2007**, *245*, 91–109. [[CrossRef](#)]
62. Campbell, I.M. *Catalysis at Surfaces*; Chapman and Hall: London, UK, 1988; p. 145.
63. Tascón, J.M.D.; González Tejuca, L. Adsorption of CO on the Perovskite-Type Oxide LaCoO_3 . *Z. Phys. Chem.* **1980**, *121*, 63–78. [[CrossRef](#)]
64. Luo, Y.; Zheng, Y.; Feng, X.; Lin, D.; Qian, Q.; Wang, X.; Zhang, Y.; Chen, Q.; Zhang, X. Controllable P Doping of the LaCoO_3 Catalyst for Efficient Propane Oxidation: Optimized Surface Co Distribution and Enhanced Oxygen Vacancies. *ACS Appl. Mater. Interfaces* **2020**, *12*, 23789–23799. [[CrossRef](#)]
65. Feng, C.; Gao, Q.; Xiong, G.; Chen, Y.; Pan, Y.; Fei, Z.; Li, Y.; Lu, Y.; Liu, C.; Liu, Y. Defect engineering technique for the fabrication of LaCoO_3 perovskite catalyst via urea treatment for total oxidation of propane. *Appl. Catal. B Environ.* **2022**, *304*, 121005. [[CrossRef](#)]
66. Yang, J.; Shi, L.; Li, L.; Fang, Y.; Pan, C.; Zhu, Y.; Liang, Z.; Hoang, S.; Li, Z.; Guo, Y. Surface modification of macroporous $\text{La}_{0.8}\text{Sr}_{0.2}\text{CoO}_3$ perovskite oxides integrated monolithic catalysts for improved propane oxidation. *Catal. Today* **2021**, *376*, 168–176. [[CrossRef](#)]
67. Nakamura, T.; Misono, M.; Yoneda, Y. Catalytic Properties of Perovskite-type Mixed Oxides, $\text{La}_{1-x}\text{Sr}_x\text{CoO}_3$. *Bull. Chem. Soc. Jpn.* **1982**, *55*, 394–399. [[CrossRef](#)]
68. Itoh, T.; Shirasaki, S.; Ofuchi, H.; Hirayama, S.; Honma, T.; Nakayama, M. Oxygen partial pressure dependence of *in situ* X-ray absorption spectroscopy at the Co and Fe K edges for $(\text{La}_{0.6}\text{Sr}_{0.4})(\text{Co}_{0.2}\text{Fe}_{0.8})\text{O}_{3-\delta}$. *Solid State Commun.* **2012**, *152*, 278–283. [[CrossRef](#)]
69. Labhassetwar, N.; Saravanan, G.; Kumar Megarajan, S.K.; Manwar, N.; Khobragade, R.; Doggali, P.; Grasset, F. Perovskite-type catalytic materials for environmental applications. *Sci. Technol. Adv. Mater.* **2015**, *16*, 036002. [[CrossRef](#)]
70. Papazisi, K.M.; Balomenou, S.; Tsiplakides, D. Synthesis and characterization of $\text{La}_{0.75}\text{Sr}_{0.25}\text{Cr}_{0.9}\text{M}_{0.1}\text{O}_3$ perovskites as anodes for CO-fuelled solid oxide fuel cells. *J. Appl. Electrochem.* **2010**, *40*, 1875–1881. [[CrossRef](#)]
71. Civera, A.; Pavese, M.; Saracco, G.; Specchia, V. Combustion synthesis of perovskite-type catalysts for natural gas combustion. *Catal. Today* **2003**, *83*, 199–211. [[CrossRef](#)]

72. Niu, J.; Deng, J.; Liu, W.; Zhang, L.; Wang, G.; Dai, H.; He, H.; Zi, X. Nanosized perovskite-type oxides $\text{La}_{1-x}\text{Sr}_x\text{MO}_{3-\delta}$ (M = Co, Mn; x = 0, 0.4) for the catalytic removal of ethylacetate. *Catal. Today* **2007**, *126*, 420–429. [[CrossRef](#)]
73. Panagiotopoulou, P.; Kondarides, D.I.; Verykios, X.E. Mechanistic Study of the Selective Methanation of CO over Ru/TiO₂ Catalyst: Identification of Active Surface Species and Reaction Pathways. *J. Phys. Chem. C* **2011**, *115*, 1220–1230. [[CrossRef](#)]

Disclaimer/Publisher's Note: The statements, opinions and data contained in all publications are solely those of the individual author(s) and contributor(s) and not of MDPI and/or the editor(s). MDPI and/or the editor(s) disclaim responsibility for any injury to people or property resulting from any ideas, methods, instructions or products referred to in the content.